Microchemical Journal 208 (2025) 112453

Contents lists available at ScienceDirect

Microchemical Journal

journal homepage: www.elsevier.com/locate/microc

Nitrophenylene-decorated V_2O_5 nanohybrids: Effect of processing conditions on enhancing the electrochemical performance for oxygen reduction reaction and dopamine sensing

Sofia Sanchez Lemus, Justin Lin, Rajeev Kumar, Obed Keelson, Amit Kumar Shringi, Fei Yan, Darlene K. Taylor, Ufana Riaz *

Department of Chemistry and Biochemistry, North Carolina Central University, Durham 27707, NC, United States

ARTICLE INFO

Keywords:
Vanadium pentoxide
Nitro-phenylene
Hybrids
Dopamine
Oxygen reduction reaction

ABSTRACT

Vanadium oxide-based nanocomposites have gained considerable interest in energy storage and electrochemical sensing due to the versatile valence states of vanadium. To enhance electrocatalytic and electrochemical sensing properties, this study focuses on the development of V_2O_5 nanohybrids with nitro-phenylene trimer, synthesized via a Suzuki coupling reaction. The electrochemical performance of both solid-state and solution-processed V_2O_5 nanohybrids was investigated, with structural and morphological properties evaluated using Fourier Transform Infrared Spectroscopy (FTIR), X-ray Diffraction (XRD), X-ray photoelectron spectroscopy (XPS), and field emission scanning electron microscopy (FE-SEM).The study revealed that the solution-processed V_2O_5/nitro-phenylene nanohybrids significantly outperformed their solid-state counterparts in both oxygen reduction reaction (ORR) applications and dopamine sensing. The solution-processed samples exhibited a $(2 + 2)e^-$ ORR pathway, resulting in increased hydrogen peroxide (H_2O_2) production compared to pristine V_2O_5. These solution-processed nanohybrids demonstrated enhanced selectivity for dopamine detection, achieving a sensitivity of 1.927 μA μM^{-1} cm^{-2} and a lower limit of detection (LOD) of 0.252 μM.

1. Introduction

The increasing demand for enhanced energy storage systems stems from the rapid progression of portable electronics, green electric vehicles, and renewable energy storage solutions [1–5]. Metal-air batteries offer a promising alternative to traditional energy storage technologies because they can be produced from accessible materials, exhibit remarkable cyclability, and provide a balance between high power and energy densities [6]. A key area of focus is the development of low-cost electrocatalysts based on transition metals. While noble metals such as platinum (Pt) or Pt-based catalysts are considered excellent cathode catalysts for the oxygen reduction reaction (ORR) due to their ability to lower activation energy, their high cost contributes significantly to the overall expense of the devices [7,8]. Therefore, research has increasingly turned towards transition metal oxides, chalcogenides, nitrides, and carbides, which not only reduce costs but also show strong potential as ORR catalysts in alkaline media, due to their high stability and enhanced catalytic activity [9,10].

Vanadium (V), comprising about 0.02 % of the earth's crust, is found in several oxidation states, such as vanadium dioxide (VO_2), vanadium trioxide (V_2O_3), and vanadium pentoxide (V_2O_5). These vanadium oxides are not only inexpensive and non-toxic but also show promising applications as electrode materials due to their high specific capacitances (Csp) and energy densities, making them suitable for use in supercapacitors and zinc-ion batteries [11,12].

Vanadium pentoxide (V_2O_5) is an exceptional material for electrochemical applications due to its layered structure, ease of synthesis, high energy density, and unique physicochemical properties [12]. This combination makes V_2O_5 a prime candidate for various energy storage and electrocatalytic systems. Its application in the selective production of hydrogen peroxide (H_2O_2) through the oxygen reduction reaction (ORR) has shown significant promise, leveraging V_2O_5's redox flexibility and layered architecture to enhance efficiency in energy storage and catalysis [12–14]. In addition to these applications, V_2O_5 has gained traction in electrochemical sensing due to its stable oxidation states ($V4^+/V5^+$), which are highly reactive to specific analytes and enhance

---

* Corresponding author.
E-mail address: uriaz@nccu.edu (U. Riaz).

https://doi.org/10.1016/j.microc.2024.112453
Received 26 August 2024; Received in revised form 6 December 2024; Accepted 10 December 2024

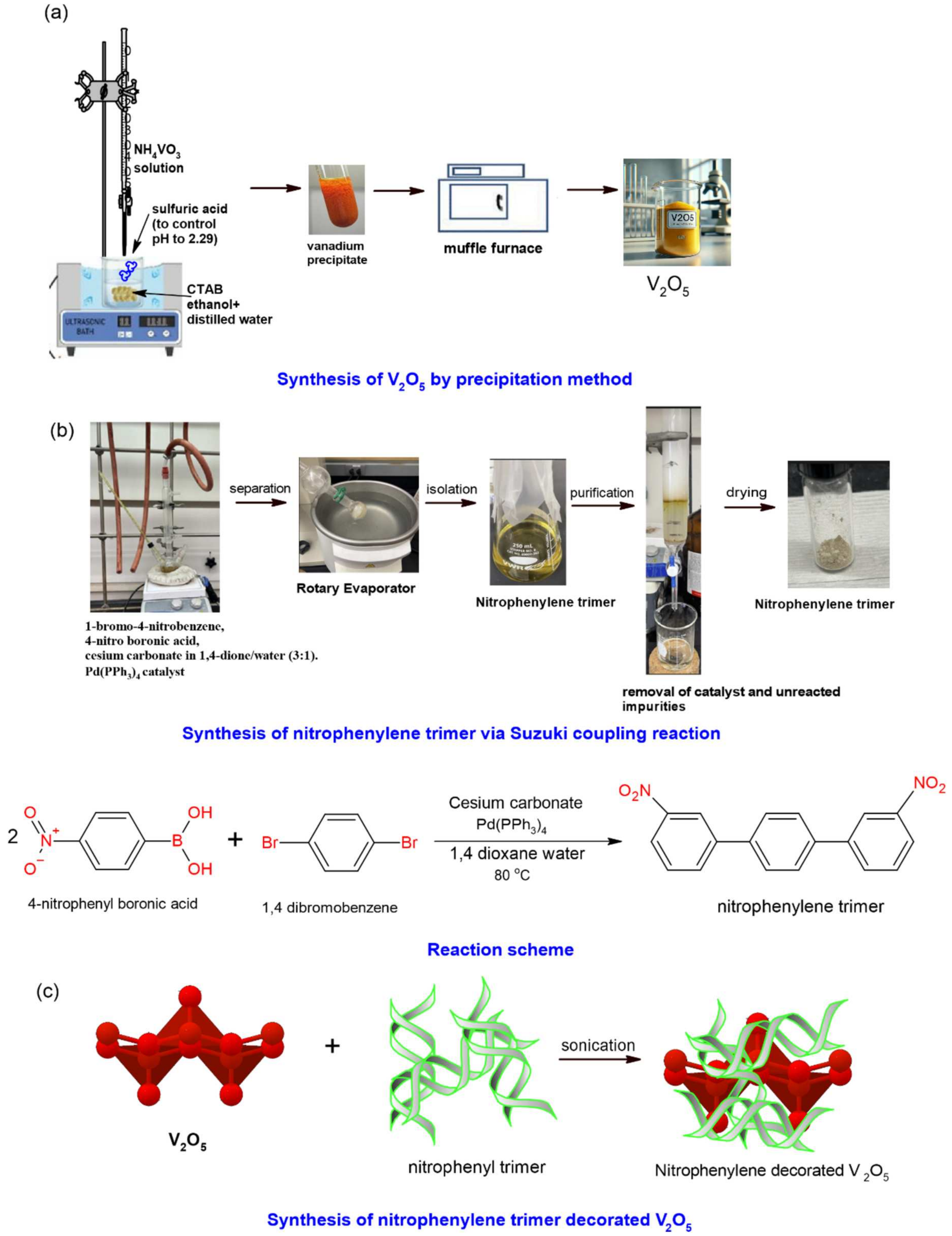

Scheme 1. Synthesis of nitrophenylene trimer decorated V_2O_5.

both sensitivity and selectivity. V_2O_5-based sensors show strong sensitivity to gases like ammonia [15], hydrogen [16], analytes like H_2O_2 and dopamine [17–20].

Despite the advantages of vanadium pentoxide (V_2O_5) in electrochemical applications, challenges such as long-term stability and sensitivity under variable conditions persist. A significant drawback of V_2O_5 as an electrode material is its poor electrical conductivity and instability during charging and discharging cycles, which results in suboptimal electrochemical cyclic performance [21,22]. Additionally, V_2O_5 is typically semiconducting, further limiting its efficacy as an electrode material. To address these challenges, incorporating conducting additives such as conducting polymers, nanomaterials, and layered carbons has emerged as a promising strategy to enhance interparticle conductivity and catalytic activity [23,24]. Various effective

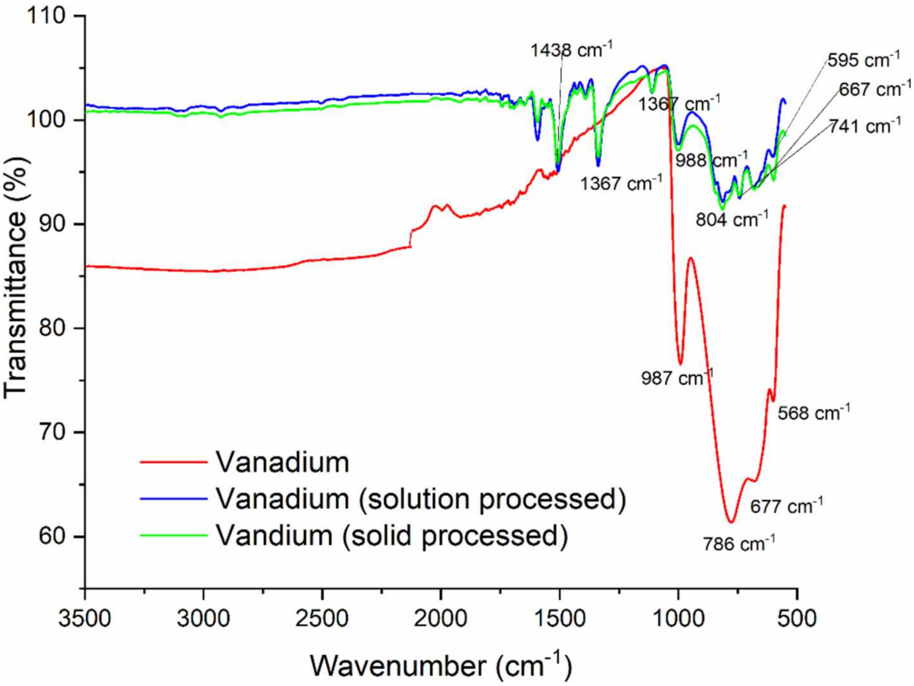

Fig. 1. FTIR spectra of V_2O_5 and V_2O_5- nitro-phenylene nanohybrids.

approaches have been explored to improve the electrochemical properties of V_2O_5, such as elemental doping [20,22,24–27], heterostructure formation [28–33], addition of graphene [34,35], reduced graphene oxide (rGO) [36], carbon nanotubes (CNTs) [37], activated carbon [38], and formulation of composites of V_2O_5 with conductive polymers [39] have been reported to enhance the optoelectronic and electrochemical properties.

It is well known that the synthesis conditions influence the composition, crystal phase and morphology of V_2O_5 which in turn effects its electrochemical performance. There are few reports in literature regarding the electrochemical performance of V_2O_5 based nanohybrids with intercalated organic moieties [10,11,40–46]. However, the comparative studies on the effect of solution and solid-state processing of the organic moieties haven't been explored. Hence, in the present study, the modification of V_2O_5 with nitro-phenylene trimer was carried out via mechanochemical and solvent-assisted routes [27,45]. Nitro-phenylene trimer was chosen for modification due to its ability to enhance the redox, catalytic, and surface properties of V_2O_5, making it a powerful functionalizing agent for applications that require robust catalytic/electrochemical sensing performance. The nitro group (–NO_2) is a strong electron-withdrawing group, which can enhance the redox properties of V_2O_5 by modifying its electronic structure. This can lead to an increase in the catalytic efficiency of V_2O_5 in various reactions, especially oxidation–reduction processes. The variation of spectral and morphological properties of the nanohybrid due to differences in the synthetic conditions was investigated via FTIR, XRD, XPS and FE-SEM studies. The electrochemical performance of vanadium pentoxide (V_2O_5) was studied in the context of both the oxygen reduction reaction (ORR) and dopamine (DA) sensing. The study specifically aimed at exploring how solution-based and solid-state processing methods impact ORR pathways, hydrogen peroxide generation, and dopamine detection efficiency. Ultimately, it seeks to optimize V_2O_5-based nanohybrids for applications in energy storage and clinical diagnostics, offering valuable insights into material modification strategies that improve electrocatalytic performance.

2. Experimental

Para-phenylene, *hexa*-ammonium heptamolybdate tetrahydrate, thiourea, 1-bromo-4-nitrobenzene, 4-nitrophenylboronic acid, 1,4-phenylene diboronic acid, 4,4′-dibromobiphenyl, tetrakis(triphenylphosphine)palladium [$Pd(PPh_3)_4$], cesium carbonate, dichloromethane, magnesium sulfate, 1,4-phenylene diboronic acid, Pd/C (10 wt% palladium), hydrazine, 1,4-dioxane, ethyl acetate, ethanol, methanol, ammonium hydroxide solution, and dimethylformamide (DMF) were obtained from Fisher Scientific and used as received without additional purification. Tetrakis(triphenylphosphine)palladium [$Pd(PPh_3)_4$], cesium carbonate, and Pd/C (10 wt% palladium) were stored in a desiccator until use.

2.1. Synthesis of V_2O_5 via precipitation method

The synthesis of V_2O_5 nanoparticles was achieved using an ultrasound-assisted precipitation method. First, 3.4 g of ammonium metavanadate (NH_4VO_3) was combined with 0.05 g of CTAB, followed by the addition of 50 ml of ethanol and 50 ml of distilled water. To adjust the pH to 2.29, 5 ml of sulfuric acid was added, and the solution was treated in an ultrasonic bath at 30 °C for 5 h. Afterward, the mixture was refluxed for 2 h at 180 °C. Once cooled to room temperature, the resulting precipitate was collected and placed in an oven at 110 °C to dry overnight. Finally, the dried sample was calcined at 600 °C for 2 h to yield the V_2O_5 nanoparticles.

2.2. Synthesis of nitro-phenylene oligomers via Suzuki coupling reaction

In a three-neck round-bottom flask equipped with a reflux condenser, nitrogen inlet, and magnetic stirrer, 1-bromo-4-nitrobenzene (1 g, 4.95 $\times 10^{-3}$ mol), 4-nitrophenylboronic acid (1.23 g, 7.43 $\times 10^{-3}$ mol), and cesium carbonate (2.41 g, 7.43 $\times 10^{-3}$ mol) were added and suspended in a 3:1 mixture of 1,4-dioxane and water. The mixture was stirred at room temperature and bubbled with nitrogen for 30 min. $Pd(PPh_3)_4$ (4.95 $\times 10^{-3}$ mol) was added as a catalyst, and the reaction was stirred at 80 °C for 16 h under a nitrogen atmosphere. Thin-layer chromatography (TLC) was used to monitor the reaction, with a mobile phase of 5

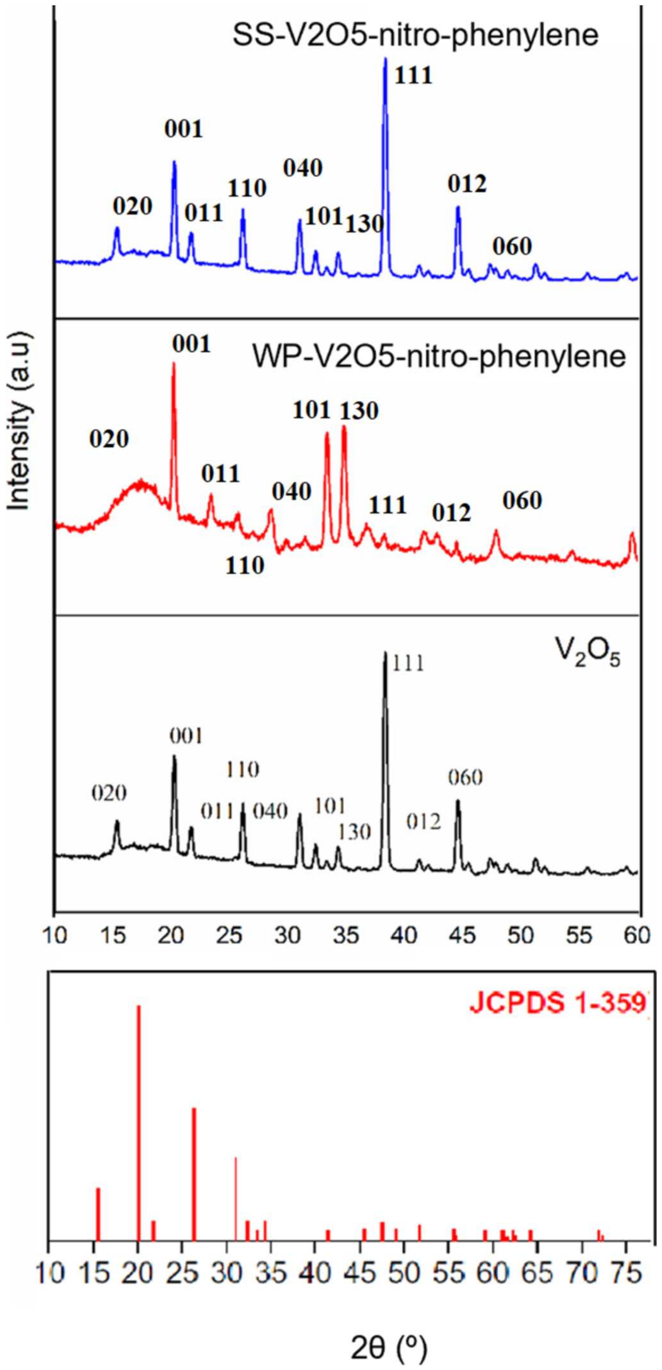

Fig. 2. XRD of V_2O_5 and V_2O_5-nitro-phenylene nanohybrids.

% ethyl acetate in hexane. Upon completion, the reaction mixture was washed with distilled water and filtered under vacuum. The residue was extracted with dichloromethane, dried over magnesium sulfate, and concentrated using a rotary evaporator. Purification was done by column chromatography on silica gel, using 5 % ethyl acetate in hexane as the eluent. The purified product was dried in a vacuum oven at 25 °C for 48 h. Structural confirmation of the product was achieved through ^{1}H-Nuclear Magnetic Resonance (NMR), Fourier-Transform Infrared Spectroscopy (FTIR), and Mass Spectroscopy (MS), with ^{1}H NMR data provided in the Supporting information as Fig. S1. Sodium sulfide was added to precipitate out palladium as a solid compound (palladium sulfide), which was filtered off.

2.3. *Preparation of nanohybrids of nitro-phenylene trimer with V_2O_5 via sonication*

For the synthesis of WP-V_2O_5-nitro-phenylene (solution-processed hybrid), 20 mg of V_2O_5 was combined with 20 mg of nitro-phenylene trimer and dispersed in 3 ml of distilled water. The mixture underwent sonication for 30 min at 30 °C. The resulting hybrid was washed with a 1:1 v/v ethanol and distilled water solution, then dried in a vacuum oven at 70 °C. For the synthesis of SS-V_2O_5-nitro-phenylene (solid-state processed hybrid), 20 mg of V_2O_5 was mixed with 20 mg of nitro-phenylene trimer and ground together using a mortar and pestle for 2 h. This hybrid was then dried in a vacuum oven at 70 °C. The reaction scheme is shown as Scheme 1.

2.4. *Structural, spectral, and morphological measurements*

FTIR spectra were taken in powder form on diamond spectrophotometer. FEI XL30 SEM-FEG Scanning Electron Microscope was used to examine the morphology and elemental mapping via Energy Dispersive X-ray (EDX) analysis. Powder X-Ray Diffraction (XRD) data were collected on a Malvern Pan analytical Empyrean diffractometer. The instrument was equipped with a copper source, operated at a voltage of 45 keV and a power of 40 kW. Patterns were obtained utilizing reflection mode and a PIXcel 3D detector. XPS experiments were performed using a Physical Electronics Versa Probe III instrument equipped with a monochromatic Al kα X-ray source ($h\nu = 1{,}486.6$ eV) and a concentric hemispherical analyzer. Charge neutralization was performed using both low energy electrons (<5 eV) and argon ions. The binding energy axis was calibrated using sputter cleaned Cu (Cu 2p3/2 = 932.62 eV, Cu 3p3/2 = 75.1 eV) and Au foils (Au 4f7/2 = 83.96 eV. Measurements were made at a takeoff angle of 45° with respect to the sample surface plane. This resulted in a typical sampling depth of 3–6 nm (95 % of the signal originated from this depth or shallower). Quantification was done using instrumental relative sensitivity factors (RSFs) that account for the X-ray cross section and inelastic mean free path of the electrons. On homogeneous samples major elements (>5 atom%) tend to have standard deviations of <3 % while minor elements can be significantly higher. The analysis size was ~200 μm in diameter.

2.5. *ORR studies*

The electrochemical measurements were performed on Waverider 200 Bipotentiostat (Pine Research). The oxygen reduction reaction (ORR) assessments were carried out in 0.1 M KOH with oxygen purging. For comparison cyclic voltammograms (CV) were also recorded under nitrogen saturation. The working electrode was a change-disk rotating ring disk electrode (RRDE) having 5 mm diameter of glassy carbon as disk electrode and Pt as the ring. The counter and reference electrodes were graphite rod and Hg/HgO, respectively. The reference electrode was calibrated against reversible hydrogen electrode (RHE) using Ar/H_2 (20 %), with Pt wires as working and counter electrodes. The calibration curve is shown in Fig. S3(a) (provided in Supporting information).

The dispersions of the samples were prepared using 5 mg of the powder material, 900 μl of isopropanol, 100 μl of DI water and 100 μl of Nafion binder (5 % in isopropanol, Sigma Aldrich). After sonication for 15 min, 10 μl of the dispersion ink was drop cast onto the disk of the RRDE and allowed to dry in the oven at 80 °C. The CV scans were recorded in the potential window of 0.5 to −1.2 V vs Hg/HgO at a scan rate of 5 mV/s in static mode. Linear sweep voltammograms (LSV) corresponding to the disk and ring currents were measured at different rotation speeds (400–2400 rpm) under continuous oxygen purging. The scan rate of 10 mV/s used for the LSV. The RRDE measurements for 10 % Pt/C are shown in Fig. S3(b) (provided in Supporting information). All potentials are converted to RHE for comparison.

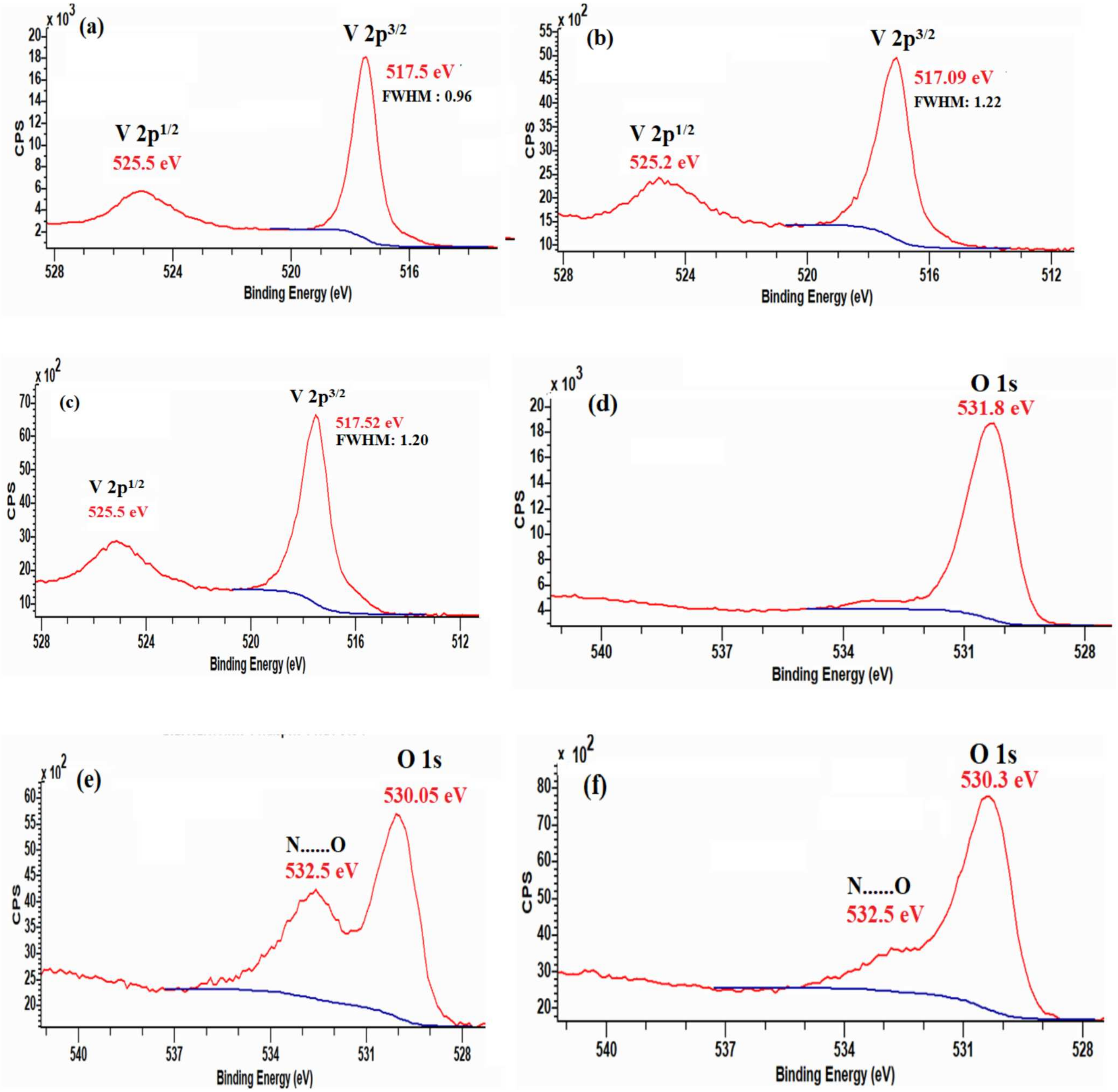

Fig. 3. (a) XPS spectra of (a) V $2p^{3/2}$ and V $2p^{1/2}$ states in V_2O_5, (b) V $2p^{3/2}$ and V $2p^{1/2}$ states V_2O_5 in WP-V_2O_5-nitro-phenylene (c) and V $2p^{3/2}$ and V $2p^{1/2}$ states in SS-V_2O_5-nitro-phenylene, (d) O 1 s in V_2O_5 (e) O 1 s in WP-V_2O_5-nitro- phenylene, (f) O 1 s in SS-V_2O_5-nitro- phenylene, (g) C 1 s in WP-V_2O_5-nitro- phenylene, (h) C 1 s in SS-V_2O_5-nitro-phenylene, (i) N1s in WP-V_2O_5-nitro- phenylene, (j) N 1 s in SS-V_2O_5-nitro- phenylene.

2.6. *Dopamine sensing*

For dopamine sensing, we used the conventional three-electrode configuration with glassy carbon electrode (3 mm diameter), platinum wire (Pt) as the counter electrode and Ag/AgCl (3.5 M KCl) as the reference electrode. The voltametric cell was placed in a cell stand (C3, BAS Inc) with controlled stirring and Ar gas purging. Cyclic voltammetry (CV), differential pulse voltammetry (DPV), and chronoamperometry (CA) signals were recorded to examine the sensing performance towards dopamine and other analytes (uric acid, NaCl, H_2O_2 and ascorbic acid). For the electrochemical measurements, 15 mL of phosphate buffer saline (PBS 1X, pH 7.4) was taken in the voltammetric cell and purged with argon gas for 30 min, with stirring at 400 rpm. During the electrochemical measurements, the stirring and purging was momentarily stopped to record the CV and DPV scans. The potential window was 0.8 to −0.9 V vs Ag/AgCl. The scan rate used was 10 mV/s. The pulse parameters for DPV, i.e., height, width, period and increment were 50 mV, 0.01 s, 0.1 s and 10 mV, respectively. The DPV scans were recorded without applying any inversion in the cathodic and anodic sweeps. The initial CV and DPV scans of the electrode, in blank electrolyte, i.e., without dopamine addition were performed, prior to sensing tests. Initially, 150 μL of dopamine from 2 μM stock solution was added. The effective concentration of dopamine in the electrolyte was 100 times lower. Purging and stirring were continued for 5 min with each addition of dopamine. The stock solutions of 2, 20, 200, 1000 and 10000 μM were used for dopamine sensing. The effective concentration at each addition of dopamine was calculated and used in the sensitivity (S) and limit of detection (LOD) evaluation.

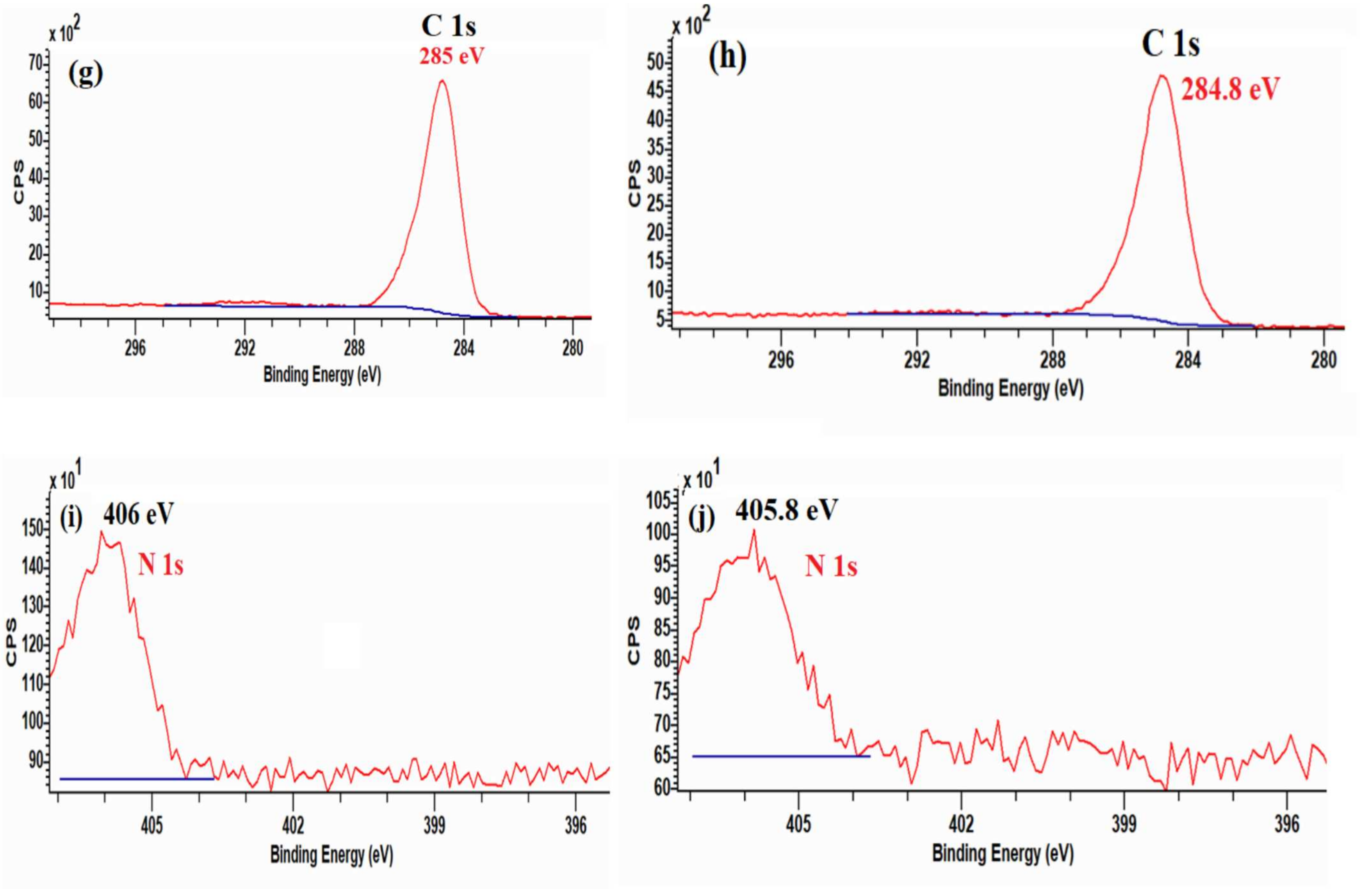

Fig. 3. (*continued*).

For the chronoamperometry tests, analytes of 100 mM concentrations (stock) were used. Since uric acid has negligible solubility in water, 0.39 mM solution of this analyte was prepared. 150 μl of these stock solutions were periodically added at 100 s time intervals. The concentration of the interferant analytes (uric acid, NaCl, dopamine and ascorbic acid) was purposefully kept high to study the efficacy of the V_2O_5 sample towards dopamine detection. Additionally, CV and DPV scans were carried out to confirm the selectivity of the samples towards dopamine.

3. Results and discussion

3.1. Spectral studies

The FTIR spectrum of V_2O_5, Fig. 1, revealed sharp peaks at 983 cm $^{-1}$, 777 cm $^{-1}$, 601 cm $^{-1}$, 568 cm $^{-1}$ due to V-O-V asymmetric stretching and V-O-V symmetric stretching vibrations respectively [39]. The FTIR spectrum of WP-V_2O_5-nitro-phenylene and SS-V_2O_5-nitro-phenylene nanohybrid, showed peaks at around 1438 cm^{-1}, 1367 cm^{-1}, 1132 cm^{-1} associated with the nitro-phenylene trimer, while the peaks of V-O-V asymmetric stretching and V-O-V symmetric stretching showed an appreciable decrease in intensity presumably due to encapsulation of the metal oxide with the polymer. The peak positions of the V-O-V in WP-V_2O_5-nitro-phenylene and SS-V_2O_5-nitro-phenylene nanohybrid were found to be similar thereby confirming that the processing conditions had no impact on the structure of V_2O_5.

3.2. XRD studies

The XRD pattern of V_2O_5 is shown in Fig. 2. The XRD peaks were well matched with the orthorhombic phase V_2O_5 with JCPDS card-no 1–359 [47]. The average crystallite size of the V_2O_5 was calculated using the Debye-Scherrer's equation and found to be 18 nm. As reported in literature, the structure of V_2O_5 is trigonal bipyramidal coordination polyhedral having oxygen (O) atom around vanadium (V) atom which are formed by the shared edges of polyhedral along (001) direction and shared corners are crossed linked along (100) direction. Distorted polyhedra have a short vanadyl bond, $[VO]^{2+}$, i.e., (1.58 Å) and at basal plane the oxygen atom is located in between the distance range of 1.78–2.02 Å. The XRD pattern of the WP-V_2O_5-nitro-phenylene and SS-V_2O_5-nitro-phenylene nanohybrid showed decrease in the peak intensities corresponding to (111) plane while, an increase in the peak intensities was noticed for the (011) plane for WP-V_2O_5-nitro-phenylene. The changes in the peaks' intensities of WP-V_2O_5-nitro-phenylene as compared to SS-V_2O_5-nitro-phenylene was presumably due to higher extent of encapsulation of the V_2O_5 by the trimer. This was established from the SEM-EDX as discussed in the preceding section.

3.3. XPS studies

The XPS survey spectra are shown as Fig. 3(a-j) and the survey spectrum are provided in Supporting information as Fig. S2(a–c). The high-resolution XPS spectra of V_2O_5 revealed peaks with binding energies 517.5 and 525.5 eV respectively, corresponding to V $2p^{3/2}$ and V $2p^{1/2}$ states Fig. 3(a) [48]. The high-resolution XPS spectra of WP-V_2O_5-nitro-phenylene and SS-V_2O_5-nitro-phenylene nanohybrid, Fig. 3(b) and (c) revealed peaks at 517 and 517.5 eV respectively, corresponding to V $2p^{3/2}$ and V $2p^{1/2}$ states. The full width at half maxima was higher for the WP-V_2O_5-nitro-phenylene and SS-V_2O_5-nitro-phenylene nanohybrids as compared to pristine V_2O_5 thereby confirming higher encapsulation of the trimer. The peak signals were found to be in the ratio of 2:1. The O 1s peak, was noticed at 530.5 eV in V_2O_5, Fig. 3(d)

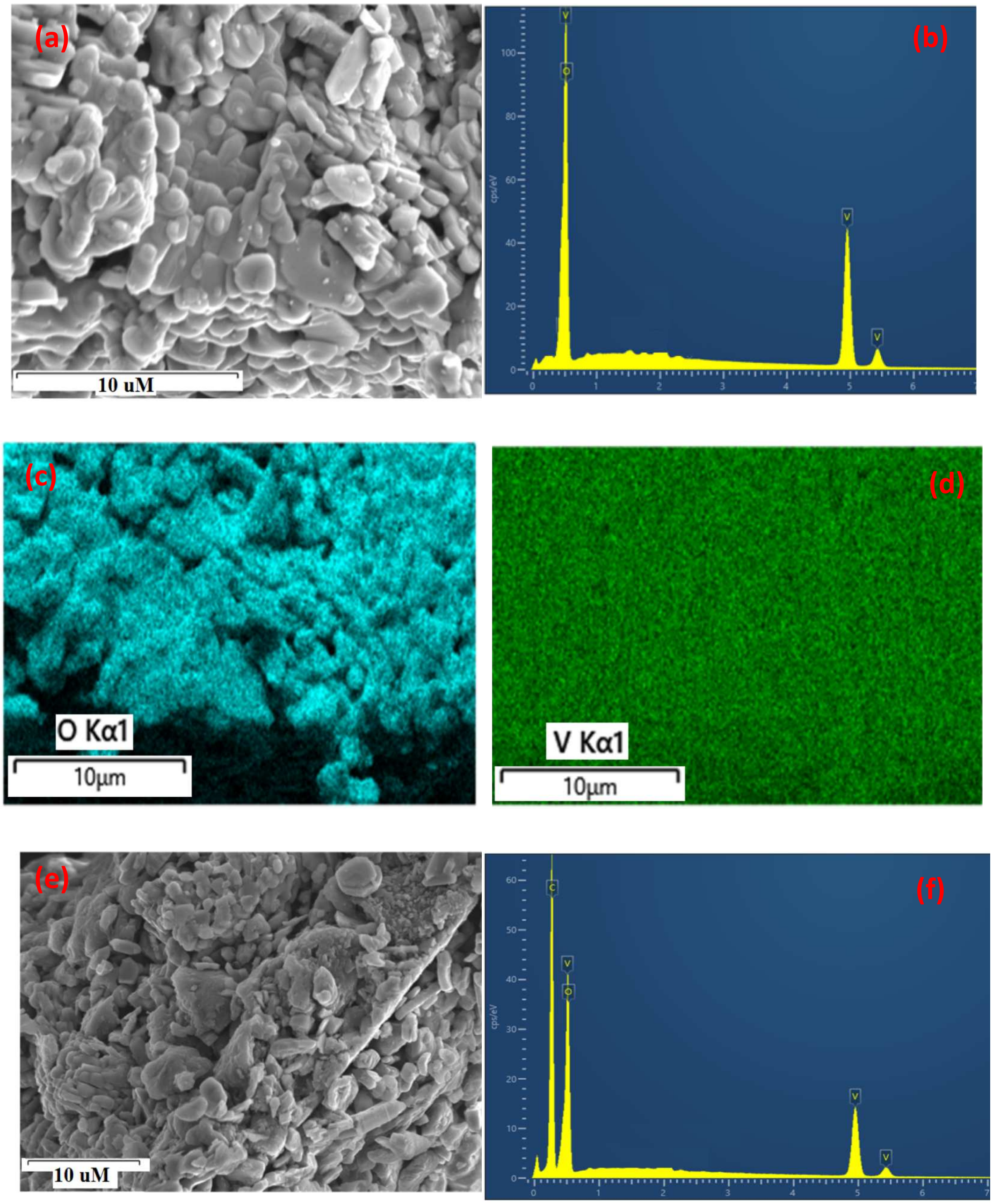

Fig. 4. (a) SEM of V_2O_5, (b) EDX of V_2O_5, and corresponding elemental mapping of (c) O, and (d) V. (e) SEM of WP-V_2O_5-nitro-phenylene, (f) EDX of WP-V_2O_5-nitro-phenylene, (g) elemental mapping of WP-V_2O_5-nitro-phenylene, and corresponding elemental mapping of (h) O, (i) V, and (j) C. (k) SEM of SS-V_2O_5-nitro-phenylene, (l) EDX of SS-V_2O_5-nitro-phenylene, (m) elemental mapping of SS-V_2O_5-nitro-phenylene, and corresponding elemental mapping of (n) O, (o) V, and (p) C.

and at 530.5 eV as well as 532.5 eV in WP-V_2O_5-nitro-phenylene and SS-V_2O_5-nitro-phenylene nanohybrids, Fig. 3(e, f). The peak at 530.5 eV was correlated to the lattice oxygen of V2O5. While the peaks at 532.5 eV observed in the nanohybrids were due to the oxygen of the nitro group present in the nitro-phenylene trimer. The peak appeared to be diffused in case of SS-V_2O_5-nitro-phenylene nanohybrid with energies of 529.7 eV and 532.1 eV. The C 1 s peak in WP-V_2O_5-nitro- phenylene and SS-V_2O_5-nitro-phenylene was noticed at 284.5 eV, Fig. 3(g, h) whereas the N 1 s peaks were noticed at 406 eV, Fig. 3(i, j). The N 1 s peak was found to be broader with FWHM to be 2.3, while in case of SS-V_2O_5-nitro-phenylene, the N 1 s peak showed a FWHM of 1.8 eV. This was also attributed to higher extent of encapsulation of the trimer in the WP-V_2O_5-nitro-phenylene as compared to SS-V_2O_5-nitro-phenylene.

3.4. SEM-EDX studies

The FE-SEM of V2O5, Fig. 4(a), shows the formation of fused rod like aggregates. From the EDX spectrum the weight percent of V:O was calculated to be 10 wt% and 50 wt% confirming the stoichiometric ratio. The atomic percent values are provided in Supporting information as Table S1. The peak intensity was also found to be higher for oxygen as compared to vanadium, Fig. 4(b). The elemental mapping showed the surface to be oxygen rich with uniform distribution of V, Fig. 4(c, d). The FE-SEM of WP-V_2O_5-nitro-phenylene, Fig. 4(e), showed a mixed

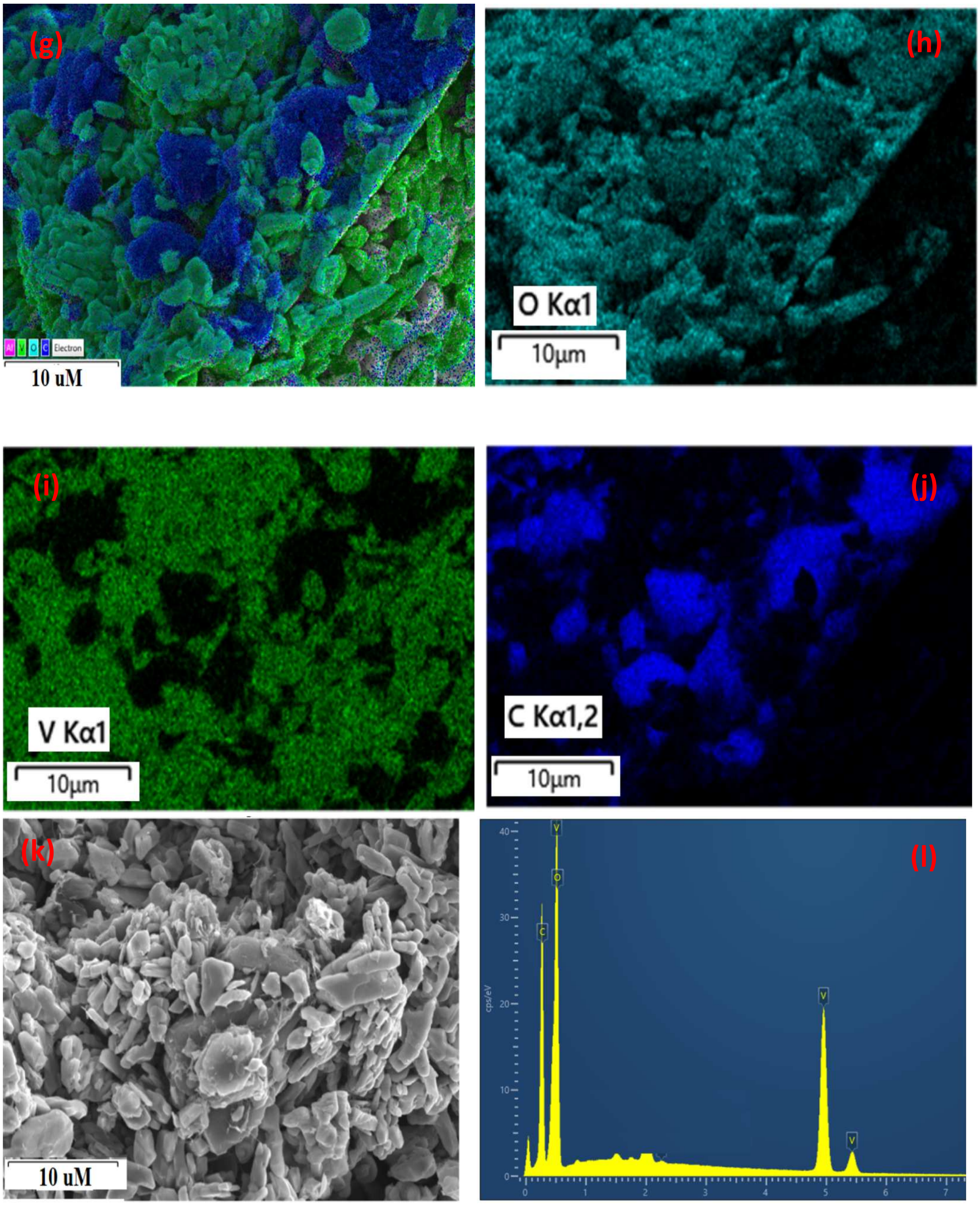

Fig. 4. (*continued*).

morphology of coral-like structures with C to be distributed uniformly over the surface of V2O5, Fig. 4(f). These clusters of the trimer appeared to be densely distributed over the surface of the V2O5, Fig. 4(g). The loading of nitro-phenylene was found to be 35 wt% as shown by the EDX spectrum, Fig. 4(f). The surface was found to be homogenously composed of V, O and C, Fig. 4(h, i, j). The FE-SEM of SS-V_2O_5-nitro-phenylene, Fig. 4(k), revealed flaky particles of V_2O_5 covered with C, Fig. 4(m). The EDX spectrum showed the C content to be 30 %, while the elemental mapping shows the surface to be intensely distributed with V and scattered distribution of nitro-phenylene, Fig. 4(n, o).

Morphological features, such as the open pores and jagged surfaces, can create localized high-energy regions that are more reactive, leading to enhanced electrocatalytic activity, better diffusion of molecules (like dopamine or oxygen) to the electroactive sites on the nanohybrids. The flat and layered nature of flaky particles on the other hand reduces the availability of high-energy surface sites, which are critical for catalysis and electrochemical sensing. Therefore, the morphological differences play a key role in the observed differences in electrochemical behavior.

3.5. *Electrochemical studies for oxygen reduction reaction (ORR)*

The ORR peak was observed in all three samples, with a reduction peak at around 0.75 to 0.40 V vs. RHE (Fig. 5(a–c)). The WP-V_2O_5-nitro-phenylene and SS-V_2O_5-nitro-phenylene nanohybrid demonstrated an earlier onset (0.70 V and 0.64 V, respectively) of the oxygen reduction reaction than the V_2O_5 sample (0.71 V). The peak current density was also higher in the hybrid samples, indicating better electrical conductivity and/or activity.

The nanohybrid samples showed higher disk currents than the V_2O_5 sample, specifically, the WP-V_2O_5-nitro-phenylene nanohybrid exhibiting the highest disk and ring currents (Fig. 5(d–f)). The increase in ring current in the trimer functionalized nanohybrids, observed in Fig. 5

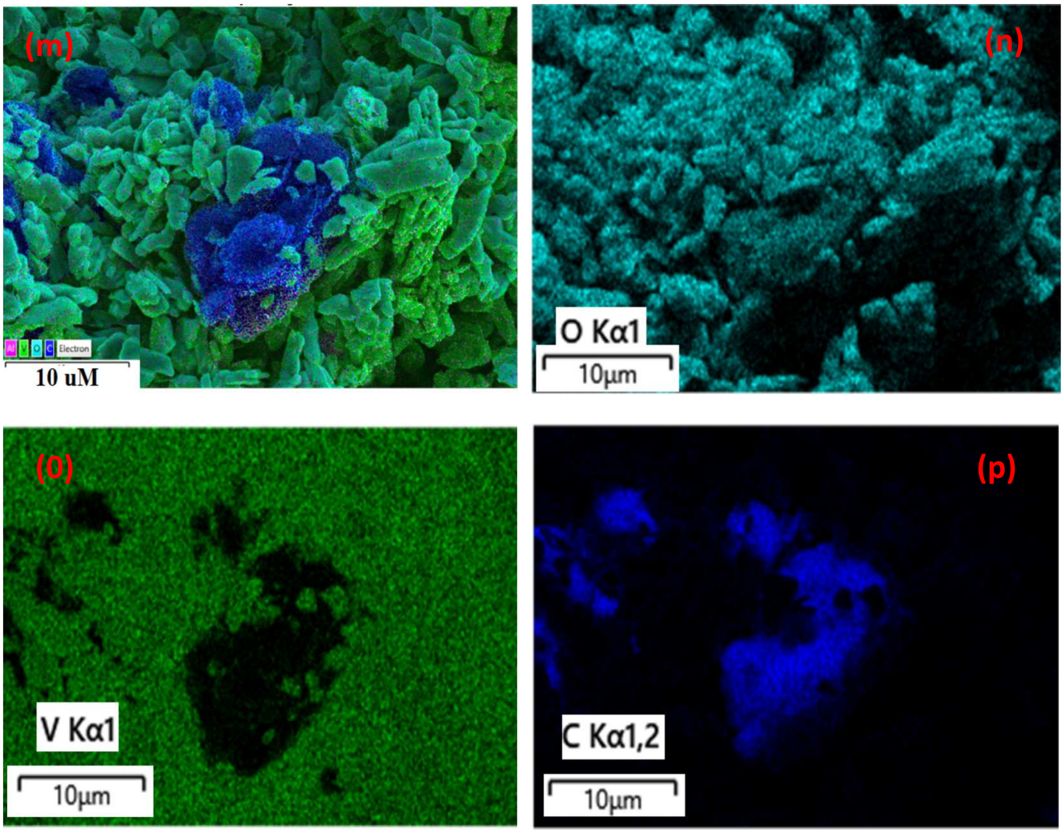

Fig. 4. (*continued*).

(d–f), indicated an increase in the production of H_2O_2. The hydrogen peroxide selectivity (p) was calculated from the values of disk current I_D, the ring current I_R, and the collection efficiency N using Eq. (1) [49]:

$$p = \frac{2\frac{I_R}{N}}{I_D + \frac{I_R}{N}} \quad (1)$$

The current collection efficiency was found to be 0.222, which is evaluated from the RRDE studies carried out in nitrogen saturated 1 mM *hexa*-amine-ruthenium (III) chloride dissolved in 0.1 M KCl.

The hydrogen peroxide selectivity was then used to calculate the number of electrons transferred, using equation (2) [50,51]:

$$n = 4 - 2(p) \quad (2)$$

The H_2O_2 yield for all three samples was calculated using Eq. (1) and are reported in Fig. 5(h). The H_2O_2 yield of the trimer functionalized nanohybrids was significantly higher than V_2O_5 within the potential range of 0.6 to 0.4 V vs RHE. For comparison, at 0.55 V the WP-V_2O_5-nitro-phenylene nanohybrid showed the highest increase in peroxide yield of 13 % when compared to the V_2O_5 sample (5 %) and the SS-V_2O_5-nitro-phenylene nanohybrid (8 %). The higher hydrogen peroxide yield in the solution-processed V_2O_5 nanohybrids is primarily due to the coral-like morphology, which increases surface area and allows for more effective electron and ion transport. This leads to a more efficient (2 + 2) e^- oxygen reduction pathway, favoring H_2O_2 production rather than the full reduction to water. Additionally, structural modifications, increased electron density, and enhanced catalytic activity contribute to the higher electrocatalytic efficiency, resulting in greater peroxide yield. The solution-processing method can facilitate better dispersion of the V_2O_5 nanohybrids in the reaction medium, ensuring that there is a higher concentration of protons (H^+) available for the reaction. This is crucial because the (2 + 2)e^- ORR pathway requires protons for the formation of hydroperoxide and hydrogen peroxide.

As a result, the solution-processed hybrids, with their more effective dispersion and structural properties, can generate more protons at the interface, leading to higher H_2O_2 yield. The peroxide yield is $>$ 50 % for the SS-V_2O_5-nitro-phenylene sample in the potential range 0.6 to 0.63 V. The number of electrons transferred (n) was calculated using equation (2) and was reported in Fig. 5 (g).

Within the potential window of 0.55 to 0.4 V, the V_2O_5 sample saw an average 'n' value of 3.92, while the nanohybrid samples saw a decrease in the average 'n' value within the same potential range, with the WP-V_2O_5-nitro-phenylene (3.80) showing a lower average 'n' value than the SS-V_2O_5-nitro-phenylene (3.88). This is consistent with the increase in H_2O_2 yield seen in the WP-V_2O_5-nitro-phenylene nanohybrid. In comparison Pt/C demonstrates 'n' value of 4 with negligible H_2O_2 formation as expected. Overall, an improvement in the kinetics for ORR is observed in the WP-V_2O_5-nitro-phenylene nanohybrid, which can be attributed to the higher extent of encapsulation of trimer in the WP-V_2O_5-nitro-phenylene compared to the SS-V_2O_5-nitro-phenylene as seen in XPS studies. Furthermore, the tolerance towards methanol poisoning is studied using chronoamperometry (Fig. 5(f). Unlike Pt/C, which is readily poisoned by methanol and thereby gets restricted for usage in direct methanol fuel cells, the V_2O_5 based samples can be useful ORR catalysts owing to their low cost and almost negligible poisoning. The onset potential and Tafel slopes values are listed in Table 1.

The higher hydrogen peroxide (H_2O_2) yield in the solution-processed V_2O_5/nitro-phenylene nanohybrids compared to solid-state processed hybrids can be attributed to several key factors, including the morphological differences, electronic structure modifications, and the reaction pathway involved in the oxygen reduction reaction (ORR). The solution-processed nanohybrids follow a (2 + 2)e^- pathway for oxygen reduction, as opposed to the more traditional (4e^- ORR pathway, which directly reduces oxygen to water (H_2O). In the (2 + 2)e^- pathway, oxygen (O_2) is first reduced to hydrogen peroxide (H_2O_2) as an intermediate product, rather than being fully reduced to water. This leads to a

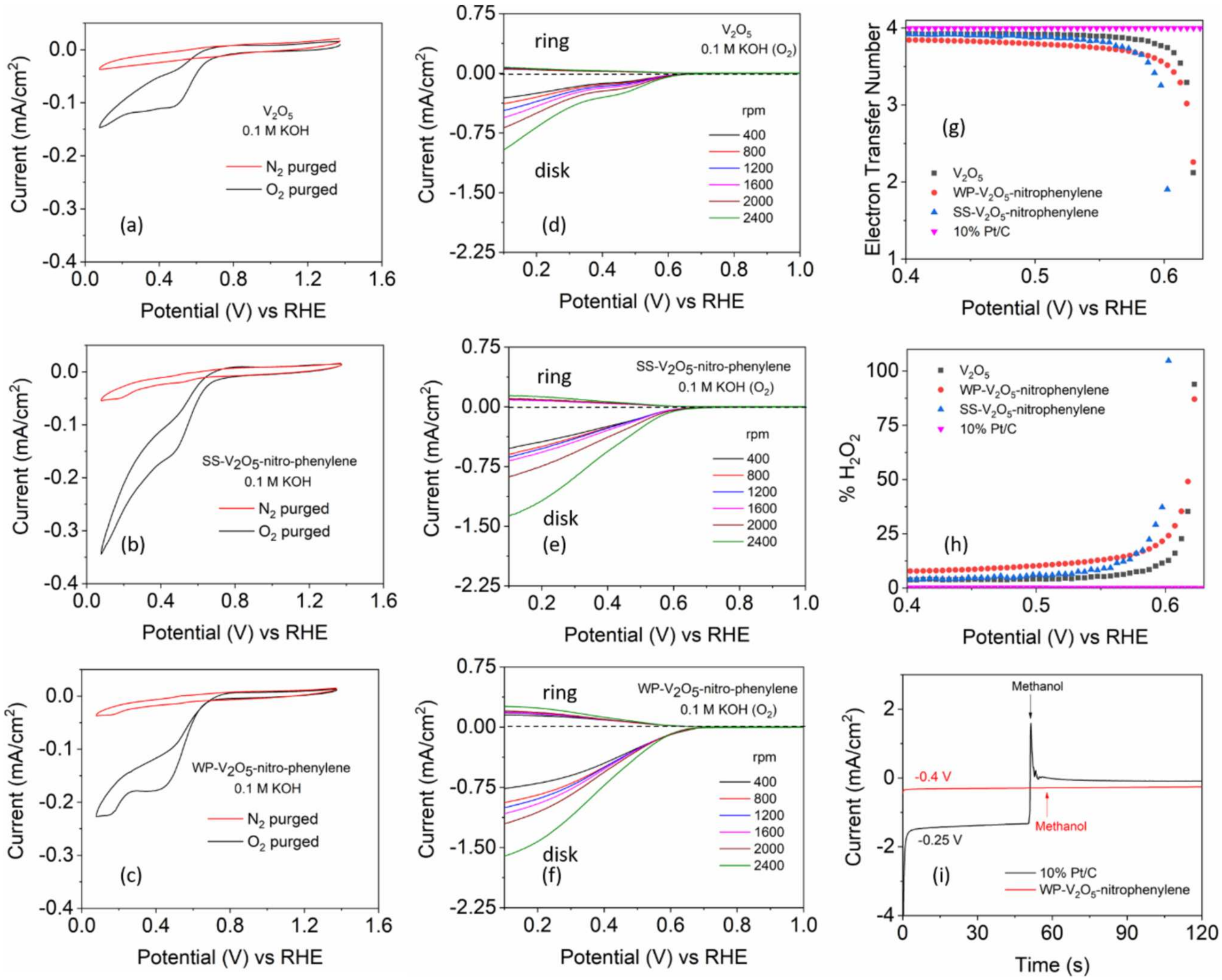

Fig. 5. CV scans in static mode under N_2 and O_2 saturation in 0.1 M KOH for (a) V_2O_5, (b) SS-V_2O_5-nitro-phenylene, and (c) WP-V_2O_5-nitro-phenylene samples. RRDE-LSV scans of (d) V_2O_5, (e) SS-V_2O_5-nitro-phenylene and (f) WP-V_2O_5-nitro-phenylene nanohybrid in 0.1 M KOH, continuously purged with O_2. (g) Electron transfer number for V_2O_5, WP-V_2O_5-nitro-phenylene, and SS-V_2O_5-nitro-phenylene nanohybrids. (d) Hydrogen peroxide generation of V_2O_5, WP-V_2O_5-nitro-phenylene, and SS-V_2O_5-nitro-phenylene nanohybrids. (f) Methanol tolerance study of WP-V_2O_5-nitro-phenylene nanohybrid.

Table 1

Comparison of the performance parameters of ORR with other reported V_2O_5 nanohybrids and recent materials.

Sample	Onset potential (V vs. RHE)	Tafel slope (mV/dec)	Reference
V_2O_5	0.74	88.30	[52]
Ag/AgCl@TiO_2/$V_2O_{5\text{-}x}$	–	64.18	[53]
Fe/rGO	0.81	105	[54]
Zn/rGO	0.76	82	[55]
ZnCu/rGO	0.79	87	[55]
Ce-ZSM-5 cal	0.81	70	[56]
Co_3O_4/SnO_2	0.77	97	[57]
V_2O_5	0.62	117	This work
SS-V_2O_5-nitro-phenylene	0.61	134	This work
WP-V_2O_5-nitro-phenylene	0.66	68	This work

higher yield of H_2O_2, as the intermediate product accumulates before further reduction. Mechanism of the $(2 + 2)e^-$ ORR can be explained on the basis that the oxygen molecule (O_2) adsorbs onto the surface of the V_2O_5 nanohybrids and One oxygen atom accepts two electrons ($2e^-$) and reacts with protons (H^+) to form hydroperoxide (O_2H^-). The hydroperoxide (O_2H^-) intermediate is further reduced by the second pair of electrons ($2e^-$) to produce hydrogen peroxide (H_2O_2). This mechanism contrasts with the ($4e^-$ pathway, where oxygen is fully reduced to water, resulting in much less hydrogen peroxide being produced. The presence of nitro-phenylene trimer could modify the electronic properties of the V_2O_5 surface, facilitating a more efficient reduction of oxygen and enhancing the formation of H_2O_2. The interactions between the V_2O_5 and the nitro-phenylene groups may also stabilize the intermediate hydroperoxide species (O_2H^-), promoting its conversion into H_2O_2 rather than further reduction to water. The solution-processing method can facilitate better dispersion of the V_2O_5 nanohybrids in the reaction medium, ensuring that there is a higher concentration of protons (H^+) available for the reaction. This is crucial because the $(2 + 2)e^-$ ORR pathway requires protons for the formation of hydroperoxide and hydrogen peroxide. As a result, the solution-processed hybrids, with their more effective dispersion and structural properties, can generate more protons at the interface, leading to higher H_2O_2 yield. Higher hydrogen peroxide yield in the solution-processed V_2O_5 nanohybrids is primarily due to the coral-like morphology, which increases surface area and allows for more effective electron and ion transport. This leads to a more efficient $(2 + 2)e^-$ oxygen reduction pathway, favoring H_2O_2 production rather than the full reduction to water. Additionally, structural modifications, increased electron density, and enhanced catalytic activity contribute to the higher electrocatalytic efficiency, resulting in greater peroxide yield.

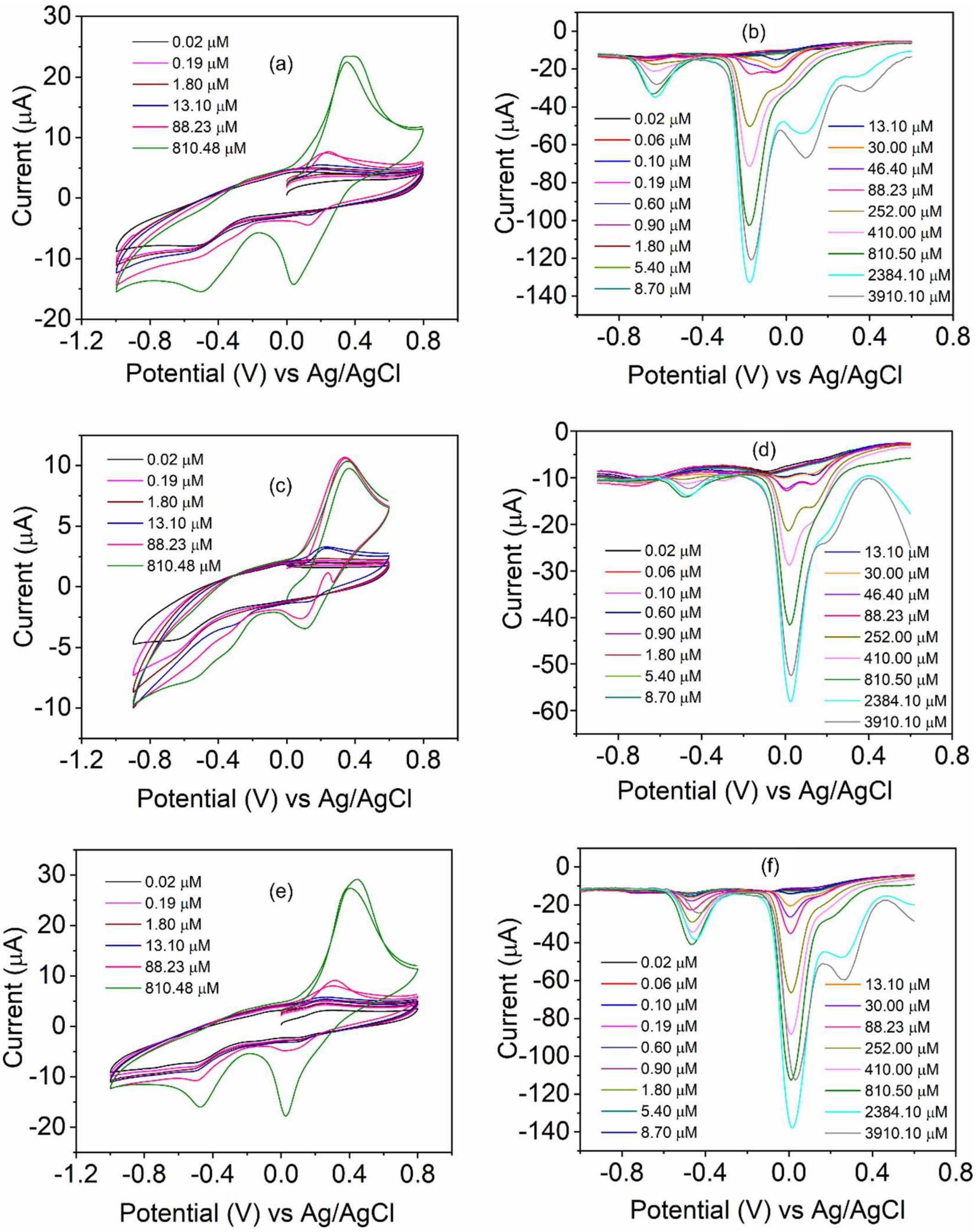

Fig. 6. Selected CV scans with dopamine addition for (a) V_2O_5, (b) SS-V_2O_5-nitro-phenylene, and (c) WP-V_2O_5-nitro-phenylene samples. DPV scans for (d) V_2O_5, (e) SS-V_2O_5-nitro-phenylene, and (f) WP-V_2O_5-nitro-phenylene samples.

3.6. Electrochemical sensing of dopamine

The CV and DPV scans (Fig. 6) reveal clear indication of the sensing ability of the V_2O_5 based samples towards dopamine. The redox peaks in CV scans were observed at 0.35 (oxidation) and 0.04 V (reduction), respectively, for pristine V_2O_5. These redox peaks in CV become visible only at high concentrations of dopamine. There is some visible shift and change in intensity of the redox peaks in case of nanohybrids. For SS-V_2O_5-nitro-phenylene, the redox peaks are observed at 0.35 and 0.11 V, while for WP-V_2O_5-nitro-phenylene the redox peaks are observed at 0.39 and 0.03 V. The additional reduction peak below −0.40 V possibly originates from the metal oxide.

The DPV technique shows much better sensitivity compared to CV [58]. The changes in the current values become significant even at low concentrations. Therefore, for the evaluation of sensitivity (S) and limit of detection (LOD), we consider the DPV scans, (provided in Supporting information as Fig. S4). The LOD and S can be obtained from the plot of the peak current with respect to the concentration of the analyte [58,59], as per the equations below.

$$\mathrm{LOD} = 3.3^{*}\left(\frac{\sigma}{k}\right) \tag{3}$$

$$S = \frac{k}{A} \tag{4}$$

where, σ is the standard deviation of the response, k is the slope of the linear plot, and A is the area of the working electrode in cm^2.

The DPV scans shows multiple peaks, and the patterns change with

Table 2
LOD and sensitivity values evaluated for the samples.

Samples	Linear range	Limit of Detection	Sensitivity	Reference
V_2O_5@PANI/GCE	6.6–110 μM	39 μM	0.015 μA μM^{-1}	[19]
Ni-doped V_2O_5/GCE	6.6–62.6 μM	0.028 μM	0.132 μA μM^{-1}	[20]
Li-doped V_2O_5/GCE	2.0–100 μM	0.1 μM	–	[60]
V_2O_5/graphene oxide/GCE	10–70 μM	0.07 μM	0.025 μA μM^{-1} cm^{-2}	[61]
VO_x@graphene/GCE	1–150 μM	0.029 μM	–	[12]
V_2O_5	10–810 μM	0.134 μM	1.662 μA μM^{-1} cm^{-2}	This work
SS-V_2O_5- nitro-phenylene	10–810 μM	0.103 μM	0.610 μA μM^{-1} cm^{-2}	This work
WP-V_2O_5- nitro-phenylene	10–810 μM	0.252 μM	1.927 μA μM^{-1} cm^{-2}	This work

increasing dopamine concentration in the electrolyte. For ease of analyses, we consider the major peak around 0 V (−0.17 V for V_2O_5) for the calculation of LOD and S. The values are provided in Table 2. The linear fits are provided in Supporting information as Fig. S5). The WP-V_2O_5-nitro-phenylene sample showed a lower limit of detection (LOD) 0.252 μM and, a higher sensitivity of 1.927 μA μM^{-1} cm^{-2} compared to the other samples.

The selectivity towards dopamine was evaluated using CV, DPV and CA, for the WP-V_2O_5- nitro-phenylene sample (Fig. 7(a, b, d)). The 150 μL of the analytes were added sequentially in the same electrolyte. Clearly, the CV and DPV techniques highlight the high selectivity towards dopamine. The chronoamperometry test was performed at 0.02 V (reduction peak in CV, Fig. 7(a)). We observe a change in current even upon addition of H_2O_2. However, this discrepancy can be due to the slight change in capacitive current. Nevertheless, the change in current is more significant for dopamine. In comparison the V_2O_5 sample also shows similar behavior (Fig. 7(c). To further verify our claim for the high selectivity of these samples towards dopamine, we carried out the DPV scans for various concentrations of H_2O_2 (provided in Supporting information as Fig. S6) and clearly observe no change in the DPV signals. Thus, the DPV and CV techniques are more confirmatory and reliable towards the selectivity test, as they explore the entire potential range (provided in Supporting information as Figs. S7–S9) [24].

4. Conclusion

The nanohybrids of V_2O_5 with nitro-phenylene trimer were successfully synthesized via solution and solid-state methods. XRD studies confirmed better encapsulation of the V_2O_5 by the trimer in the solution state as compared to solid state synthesis. This was established from the SEM-EDS discussed in the proceeding section. The loading of nitro-phenylene was found to be 35 wt% for solution processed V_2O_5-nitro-phenylene and 30 wt% for solid state processed V_2O_5-nitro-phenylene. The study demonstrates that the solution-processed V_2O_5/nitro-phenylene nanohybrids exhibit significantly enhanced electrochemical performance compared to their solid-state counterparts, particularly in applications such as the oxygen reduction reaction (ORR) and dopamine

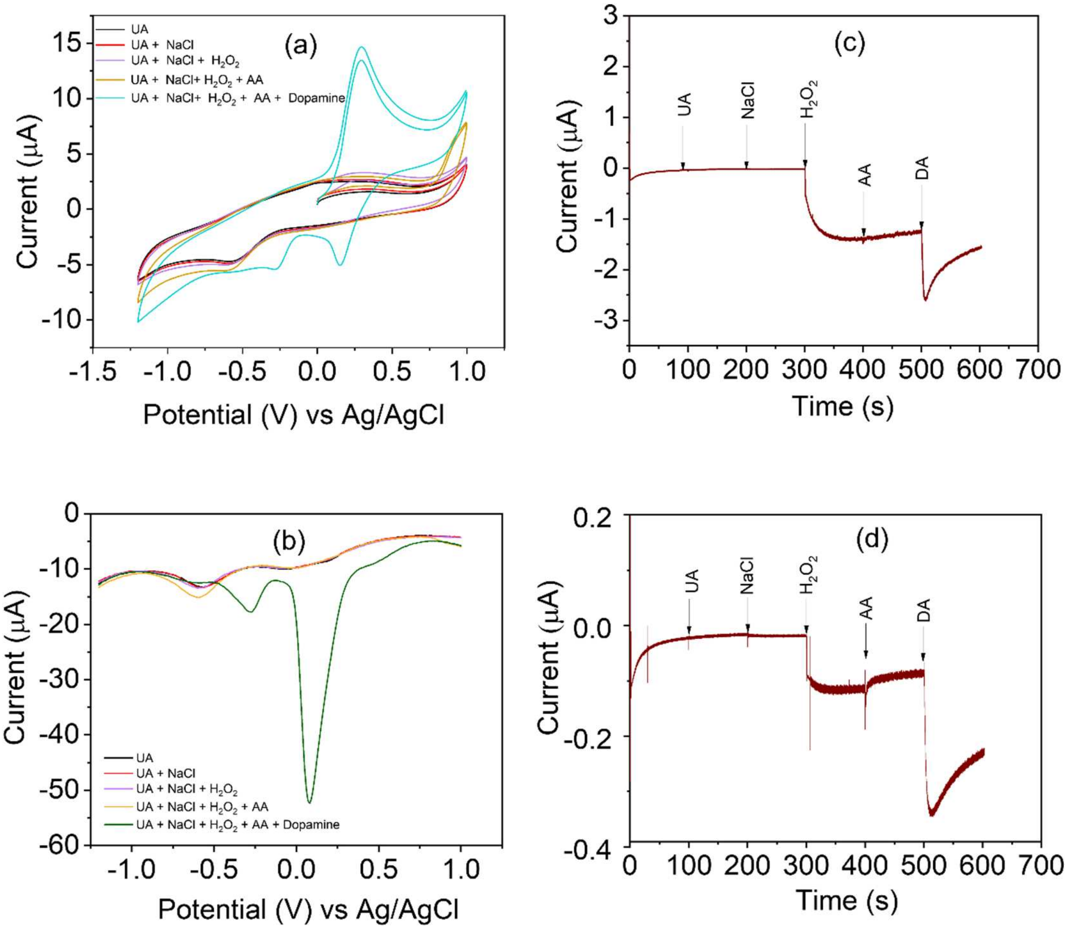

Fig. 7. (a) CV and (b) DPV scans with incremental addition of different analytes (100 mM stock) for the selectivity test. Chronoamperometry tests with different analytes (100 mM stock) for (c) V_2O_5 and (d) WP-V_2O_5- nitro-phenylene samples. 150 μL was added each time in 15 ml PBS 1X.

sensing. The superior performance of the solution-processed nanohybrids can be attributed to their coral-like morphology, which provides a larger surface area and improved electron and ion transport, crucial factors for efficient electrocatalysis and enhanced sensor sensitivity. This structure promotes a $(2 + 2)e^-$ ORR pathway, leading to increased hydrogen peroxide (H_2O_2) production, which is advantageous for various electrocatalytic and sensing applications. In addition to morphology, the interaction between V_2O_5 and nitro-phenylene trimer likely contributes to the enhanced electrocatalytic activity by modifying the electronic properties of the material and stabilizing intermediate species, thereby facilitating more efficient reduction reactions. The solution-processing method also ensures better dispersion and availability of active sites, further improving the selectivity and sensitivity for dopamine detection, with a low detection limit and high sensitivity. He solution-processed V_2O_5/nitro-phenylene nanohybrids show great promise for a range of applications, including electrocatalysis, energy storage, and biosensing, where high efficiency, selectivity, and sensitivity are essential. The findings underline the importance of morphological design and material processing in tailoring the properties of nanomaterials for advanced electrochemical applications.

CRediT authorship contribution statement

Sofia Sanchez Lemus: . **Justin Lin:** Investigation. **Rajeev Kumar:** Resources, Formal analysis. **Obed Keelson:** Investigation. **Amit Kumar Shringi:** . **Fei Yan:** Resources. **Darlene K. Taylor:** Methodology, Funding acquisition. **Ufana Riaz:** Writing – review & editing, Writing – original draft, Supervision.

Declaration of competing interest

The authors declare that they have no known competing financial interests or personal relationships that could have appeared to influence the work reported in this paper.

Acknowledgement

The authors wish to acknowledge National Science Foundation (Award # 2122044), the NSF PREM for Hybrid Nanoscale Systems between NCCU and Penn State for providing financial assistance.

Appendix A. Supplementary data

Supplementary data to this article can be found online at https://doi.org/10.1016/j.microc.2024.112453.

Data availability

Data will be made available on request.

References

[1] D. Qi, Y. Liu, Z. Liu, L. Zhang, X. Chen, Design of Architectures and Materials in In-Plane Micro-supercapacitors: Current Status and Future Challenges, Adv. Mater. 29 (2017) 1602802, https://doi.org/10.1002/adma.201602802.

[2] X. Dai, F. Wan, L. Zhang, H. Cao, Z. Niu, Freestanding graphene/VO_2 composite films for highly stable aqueous Zn-ion batteries with superior rate performance, Energy Storage Mater. 17 (2019) 143–150, https://doi.org/10.1016/j.ensm.2018.07.022.

[3] E. Fan, L. Li, Z. Wang, J. Lin, Y. Huang, Y. Yao, R. Chen, F. Wu, Sustainable Recycling Technology for Li-Ion Batteries and Beyond: Challenges and Future Prospects, Chem. Rev. 120 (2020) 7020–7063, https://doi.org/10.1021/acs.chemrev.9b00535.

[4] S. Ramesh, A.T.A. Ahmed, Y. Haldorai, V. Kakani, C. Bathula, H.S. Kim, Cobalt sulfide@cobalt-metal organic frame works materials for energy storage and electrochemical glucose detection sensor application, J. Alloy. Compd. 967 (2023) 171760, https://doi.org/10.1016/j.jallcom.2023.171760.

[5] J.W. Gittins, Y. Chen, S. Arnold, V. Augustyn, A. Balducci, T. Brousse, E. Frackowiak, P. Gómez-Romero, A. Kanwade, L. Köps, P.K. Jha, D. Lyu, M. Meo, D. Pandey, L. Pang, V. Presser, M. Rapisarda, D. Rueda-García, S. Saeed, P. M. Shirage, A. Ślesiński, F. Soavi, J. Thomas, M.-M. Titirici, H. Wang, Z. Xu, A. Yu, M. Zhang, A.C. Forse, Interlaboratory study assessing the analysis of supercapacitor electrochemistry data, J. Power Sources 585 (2023) 233637, https://doi.org/10.1016/j.jpowsour.2023.233637.

[6] R. Kumar, S. Kumar, S.G. Chandrappa, N. Goyal, A. Yadav, N. Ravishankar, A. S. Prakash, B. Sahoo, Nitrogen-doped carbon nanostructures embedded with Fe-Co-Cr alloy based nanoparticles as robust electrocatalysts for Zn-air batteries, J. Alloy. Compd. 984 (2024) 173862, https://doi.org/10.1016/j.jallcom.2024.173862.

[7] J. Hui, L. Ruiyi, D. Zhenzhong, G. Xiaoyan, X. Junshan, S. Jinsong, L. Zaijun, Platinum nanoparticle-graphene quantum dot nanocage as a promising Schottky heterojunction electrocatalyst for electrochemical detection of vanillin in baby milk powder, Microchem. J. 186 (2023) 108320, https://doi.org/10.1016/j.microc.2022.108320.

[8] R.M. Abdel Hameed, S.S. Medany, Construction of core-shell structured nickel@platinum nanoparticles on graphene sheets for electrochemical determination of nitrite in drinking water samples, Microchem. J. 145 (2019) 354–366, https://doi.org/10.1016/j.microc.2018.10.045.

[9] S. Wang, L. Wu, H. Zhang, Z. Wang, Q. Qin, X. Wang, Y. Lu, L. Li, M. Li, Facile Synthesis of Two Dimensional (2D) V_2O_5 Nanosheets Film towards Photodetectors, Materials 15 (2022) 8313, https://doi.org/10.3390/ma15238313.

[10] Y. Zhu, X. Liu, X. Hu, T. Wang, I.P. Parkin, M. Wang, B.D. Boruah, Polyaniline and water pre-intercalated V_2O_5 cathodes for high-performance planar zinc-ion micro-batteries, Chem. Eng. J. 487 (2024) 150384, https://doi.org/10.1016/j.cej.2024.150384.

[11] J. Sun, Y. Zhao, Y. Liu, H. Jiang, C. Huang, M. Cui, T. Hu, C. Meng, Y. Zhang, "Three-in-One" Strategy that Ensures $V_2O_5\cdot n\,H_2O$ with Superior Zn $^{2+}$ Storage by Simultaneous Protonated Polyaniline Intercalation and Encapsulation, Small Struct. 3 (2022) 2100212, https://doi.org/10.1002/sstr.202100212.

[12] S. Zhang, G. Feng, Z. Bao, X. Peng, C. Jiang, Y. Shao, S. Wang, J. Wang, Oxygen Vacancy Boosts the V_2O_5 Performance for the Electrochemical H_2O_2 Product, Ind. Eng. Chem. Res. (2023) acs.iecr.3c00262, https://doi.org/10.1021/acs.iecr.3c00262.

[13] C.J. Verma, A. Kumar, R.P. Ojha, R. Prakash, Au-V_2O_5/Polyindole composite: An approach for ORR in different electrolytes, J. Electroanal. Chem. 861 (2020) 113959, https://doi.org/10.1016/j.jelechem.2020.113959.

[14] S. Sekar, I. Rabani, C. Bathula, S. Kumar, S. Govindaraju, K. Yun, Y.-S. Seo, D. Y. Kim, S. Lee, Graphitic carbon-encapsulated V_2O_5 nanocomposites as a superb photocatalyst for crystal violet degradation, Environ. Res. 205 (2022) 112201, https://doi.org/10.1016/j.envres.2021.112201.

[15] N. Duc Phuong Nam, D. Thi Huong, P. Hai Anh, B. Xuan Hoang, L. Huu Phuoc, N. Thanh Nghi, L. Khac Hoang, D. Duc Vuong, V. Xuan Hien, Microwave-synthesized V_2O_5 nanoparticles for ammonia sensing at room temperature, Mater. Sci. Eng.: B 307 (2024) 117533, https://doi.org/10.1016/j.mseb.2024.117533.

[16] N. Panahi, M. Shirazi, M.T. Hosseinnejad, Fabrication, characterization and hydrogen gas sensing performance of nanostructured V_2O_5 thin films prepared by plasma focus method, J. Mater. Sci. Mater. Electron. 29 (2018) 13345–13353, https://doi.org/10.1007/s10854-018-9459-4.

[17] J. Sun, C. Li, Y. Qi, S. Guo, X. Liang, Optimizing Colorimetric Assay Based on V_2O_5 Nanozymes for Sensitive Detection of H_2O_2 and Glucose, Sensors 16 (2016) 584, https://doi.org/10.3390/s16040584.

[18] X. Zhu, Y. Xue, S. Han, W. Chen, M. Fu, Y. Gao, S. Nie, Q. Liu, X. Zhang, X. Zhang, V_2O_5-montmorillonite nanocomposites of peroxidase-like activity and their application in the detection of H_2O_2 and glutathione, Appl. Clay Sci. 195 (2020) 105718, https://doi.org/10.1016/j.clay.2020.105718.

[19] R. Suresh, K. Giribabu, R. Manigandan, S.P. Kumar, S. Munusamy, S. Muthamizh, V. Narayanan, Characterization and dopamine sensing property of V_2O_5@polyailine nanohybrid, Synth. Met. 196 (2014) 151–157, https://doi.org/10.1016/j.synthmet.2014.07.025.

[20] R. Suresh, K. Giribabu, R. Manigandan, S.P. Kumar, S. Munusamy, S. Muthamizh, A. Stephen, V. Narayanan, New electrochemical sensor based on Ni-doped V_2O_5 nanoplates modified glassy carbon electrode for selective determination of dopamine at nanomolar level, Sens. Actuators, B 202 (2014) 440–447, https://doi.org/10.1016/j.snb.2014.05.095.

[21] E.G. Tolstopyatova, M.A. Kamenskii, V.V. Kondratiev, Vanadium Oxide–Conducting Polymers Composite Cathodes for Aqueous Zinc-Ion Batteries: Interfacial Design and Enhancement of Electrochemical Performance, Energies 15 (2022) 8966, https://doi.org/10.3390/en15238966.

[22] W. Young Jang, Ch. Venkata Reddy, A. Daouli, R.R. Kakarla, N. Bandaru, J. Shim, M. Badawi, T.M. Aminabhavi, Novel 2D sulfur-doped V_2O_5 flakes and their applications in photoelectrochemical water oxidation and high-performance energy storage supercapacitors, Chem. Eng. J. 461 (2023) 141935, https://doi.org/10.1016/j.cej.2023.141935.

[23] C. Xiong, A.E. Aliev, B. Gnade, K.J. Balkus, Fabrication of Silver Vanadium Oxide and V_2O_5 Nanowires for Electrochromics, ACS Nano 2 (2008) 293–301, https://doi.org/10.1021/nn700261c.

[24] Y. Wei, C.-W. Ryu, K.-B. Kim, Improvement in electrochemical performance of V_2O_5 by Cu doping, J. Power Sources 165 (2007) 386–392, https://doi.org/10.1016/j.jpowsour.2006.12.016.

[25] M. Tamilselvan, T.V. Madhukar Sreekanth, K. Yoo, J. Kim, Self-doped 2D-V_2O_5 nanoflakes – A high electrochemical performance cathode in rechargeable zinc ion batteries, Ceram. Int. 47 (2021) 29832–29839, https://doi.org/10.1016/j.ceramint.2021.07.156.

[26] V. Uma Shankar, D. Govindarajan, P. Christuraj, M.J. Salethraj, F.J. Johanson, M. D. Raja, Enhanced the electrochemical properties of Ni doped V2O5 as a electrode material for supercapacitor applications, Mater. Today: Proc. 50 (2022) 2675–2678, https://doi.org/10.1016/j.matpr.2020.08.213.

[27] L. Sajeev, C. Sreelakshmi, M.R. Charlotte, A.M. Manoj, C.K. Subramaniam, N.A. N. Raj, B. Rajeswaran, L.R. Viannie, Study of structural and electrochemical properties of tungsten-doped V_2O_5 nanostructures for solid state energy storage applications, J. Mater. Sci. Mater. Electron. 33 (2022) 24159–24172, https://doi.org/10.1007/s10854-022-09103-x.

[28] A. Mirmohseni, M.S.S. Dorraji, M.G. Hosseini, Influence of metal oxide nanoparticles on pseudocapacitive behavior of wet-spun polyaniline-multiwall carbon nanotube fibers, Electrochim. Acta 70 (2012) 182–192, https://doi.org/10.1016/j.electacta.2012.03.100.

[29] Y. Wang, T. Lubbers, R. Xia, Y.-Z. Zhang, M. Mehrali, M. Huijben, J.E. Ten Elshof, Printable Two-Dimensional V_2O_5/MXene Heterostructure Cathode for Lithium-Ion Battery, J. Electrochem. Soc. 168 (2021) 020507, https://doi.org/10.1149/1945-7111/abdef2.

[30] J. Wang, F. Zheng, M. Li, J. Wang, D. Jia, X. Mao, P. Hu, Q. Zhen, Y. Yu, V_2O_5@RuO_2 core–shell heterojunction nano-arrays as electrode material for supercapacitors, Chem. Eng. J. 446 (2022) 136922, https://doi.org/10.1016/j.cej.2022.136922.

[31] Z. Yang, X. Xie, Z. Zhang, J. Yang, C. Yu, S. Dong, M. Xiang, H. Qin, NiS_2@V_2O_5/VS_2 ternary heterojunction for a high-performance electrocatalyst in overall water splitting, Int. J.Hydrogen Energy 47 (2022) 27338–27346, https://doi.org/10.1016/j.ijhydene.2022.06.076.

[32] T.-F. Hou, M.A. Johar, R. Boppella, M.A. Hassan, S.J. Patil, S.-W. Ryu, D.-W. Lee, Vertically aligned one-dimensional ZnO/V_2O_5 core–shell hetero-nanostructure for photoelectrochemical water splitting, J. Energy Chem. 49 (2020) 262–274, https://doi.org/10.1016/j.jechem.2020.02.004.

[33] M. Arunachalam, K.-S. Ahn, S.H. Kang, Oxygen evolution NiOOH catalyst assisted V_2O_5@$BiVO_4$ inverse opal hetero-structure for solar water oxidation, Int. J. Hydrogen Energy 44 (2019) 4656–4663, https://doi.org/10.1016/j.ijhydene.2019.01.024.

[34] Q. Wu, Y. Xu, Z. Yao, A. Liu, G. Shi, Supercapacitors Based on Flexible Graphene/Polyaniline Nanofiber Composite Films, ACS Nano 4 (2010) 1963–1970, https://doi.org/10.1021/nn1000035.

[35] Q. Ke, J. Wang, Graphene-based materials for supercapacitor electrodes – A review, J. Materiomics 2 (2016) 37–54, https://doi.org/10.1016/j.jmat.2016.01.001.

[36] J. Hwang, H.M. Kim, S. Shin, Y. Sun, Designing a High-Performance Lithium–Sulfur Batteries Based on Layered Double Hydroxides–Carbon Nanotubes Composite Cathode and a Dual-Functional Graphene–Polypropylene–Al_2O_3 Separator, Adv. Funct. Mater. 28 (2018) 1704294, https://doi.org/10.1002/adfm.201704294.

[37] M. Sathiya, A.S. Prakash, K. Ramesha, J.M. Tarascon, A.K. Shukla, V_2O_5-anchored carbon nanotubes for enhanced electrochemical energy storage, J. Am. Chem. Soc. 133 (2011) 16291–16299, https://doi.org/10.1021/ja207285b.

[38] A.G. Pandolfo, A.F. Hollenkamp, Carbon properties and their role in supercapacitors, J. Power Sources 157 (2006) 11–27, https://doi.org/10.1016/j.jpowsour.2006.02.065.

[39] K. Gurunathan, A.V. Murugan, R. Marimuthu, U.P. Mulik, D.P. Amalnerkar, Electrochemically synthesised conducting polymeric materials for applications towards technology in electronics, optoelectronics and energy storage devices, Mater. Chem. Phys. 61 (1999) 173–191, https://doi.org/10.1016/S0254-0584(99)00081-4.

[40] K. Li, C. Liu, J. Lv, T. Cao, Y. Zhang, Y. Gong, L. Zheng, Organic Species-Intercalated Vanadium Oxide for Sodium-Ion Battery: Mixed-Anion Coordination Effect, Enhanced *d* - *p* Orbital Hybridization, and Topotactic Phase Conversion Induced by N-Substitution, Inorg. Chem. 62 (2023) 20105–20119, https://doi.org/10.1021/acs.inorgchem.3c02974.

[41] A.V. Murugan, B.B. Kale, C.-W. Kwon, G. Campet, K. Vijayamohanan, Synthesis and characterization of a new organo–inorganic poly(3,4-ethylene dioxythiophene) PEDOT/ V_2O_5 nanocomposite by intercalation, J. Mater. Chem. 11 (2001) 2470–2475, https://doi.org/10.1039/b100714i.

[42] T. Nakato, I. Kato, K. Kuroda, C. Kato, Preparation of V_2O_5 gel-viologen intercalation compounds, J. Colloid Interface Sci. 133 (1989) 447–451, https://doi.org/10.1016/S0021-9797(89)80055-4.

[43] M. Clites, E. Pomerantseva, Organic/Inorganic Hybrid Layered Electrodes Via Chemical Pre-Intercalation Approach for Intercalation Cathodes, Meet. Abstr. (2018) 452, https://doi.org/10.1149/MA2018-01/3/452.

[44] Z.F. Li, E. Ruckenstein, Intercalation of Conductive Polyaniline in the Mesostructured V_2O_5, Langmuir 18 (2002) 6956–6961, https://doi.org/10.1021/la0203887.

[45] J. Zhang, S. Liu, S. Zhou, H. Liu, R. Ding, S. Wei, Z. Wang, X. Lu, Novel Inorganic–Organic Hybrid Cathode for Aqueous Zinc-Ion Batteries: V_2O_5 Pillared with Diethylenetriamine like a Double-Stud, ACS Sustain. Chem. Eng. 10 (2022) 10243–10251, https://doi.org/10.1021/acssuschemeng.2c01975.

[46] Y. Liu, T. Wang, Y. Sun, M. Zhang, G. Gao, J. Yang, K. Cai, Fast and efficient in-situ construction of low crystalline PEDOT-intercalated V_2O_5 nanosheets for high-performance zinc-ion battery, Chem. Eng. J. 484 (2024) 149501, https://doi.org/10.1016/j.cej.2024.149501.

[47] M. Shashank, F.A. Alharthi, A. Alsalme, N. Al-Zaqri, G. Nagaraju, Ag decorated V_2O_5 nanorods as cathode material for lithium ion battery, J. Mater. Sci. Mater. Electron. 31 (2020) 14279–14286, https://doi.org/10.1007/s10854-020-03984-6.

[48] J. Zia, J. Kashyap, U. Riaz, Facile synthesis of polypyrrole encapsulated V_2O_5 nanohybrids for visible light driven green sonophotocatalytic degradation of antibiotics, J. Mol. Liq. 272 (2018) 834–850, https://doi.org/10.1016/j.molliq.2018.10.091.

[49] R. Nivetha, M.R. Asrami, R. Kumar, S. Sharma, M. Jourshabani, R.D. Kumar, S. Ravichandran, B. Lee, Y. Lee, J.S. Chung, S.G. Kang, W.M. Choi, S.H. Hur, Highly Immobilized Bimetallic Fe/M-N4 (M- Mg or Zn) Conductive Metal–Organic Frameworks on Nitrogen-Doped Porous Carbon for Efficient Electrocatalytic Hydrogen Evolution and Oxygen Reduction Reactions, Small Struct. 5 (2024) 2300355, https://doi.org/10.1002/sstr.202300355.

[50] S. Kumar, R. Kumar, N. Goyal, A. Vazhayil, A. Yadav, N. Thomas, B. Sahoo, N-Doped Carbon Nanotubes Nucleated through Cobalt Nanoparticles as Bifunctional Catalysts for Zinc-Air Batteries, ACS Appl. Nano Mater. 7 (2024), https://doi.org/10.1021/acsanm.4c00479.

[51] R. Zhou, Y. Zheng, M. Jaroniec, S.-Z. Qiao, Determination of the Electron Transfer Number for the Oxygen Reduction Reaction: From Theory to Experiment, ACS Catal. 6 (2016) 4720–4728, https://doi.org/10.1021/acscatal.6b01581.

[52] Z. Feng, Y. Zhang, Y. Zhao, J. Sun, Y. Liu, H. Jiang, M. Cui, T. Hu, C. Meng, Dual intercalation of inorganics–organics for synergistically tuning the layer spacing of $V_2O_{5}\cdot n\,H_2O$ to boost Zn^{2+} storage for aqueous zinc-ion batteries, Nanoscale 14 (2022) 8776–8788, https://doi.org/10.1039/D2NR02122F.

[53] X. Zhang, J. Wang, X. Lang, T. Wang, T. Qu, Q. Lai, L. Li, C. Yao, K. Cai, A novel mulberry-like Ag/AgCl@TiO_2/V_2O_{5-x} composite as a stable catalyst for long-life potassium-oxygen batteries, J. Storage Mater. 75 (2024) 109590, https://doi.org/10.1016/j.est.2023.109590.

[54] J. Milikić, A. Nastasić, L. Rakočević, K. Radinović, S. Stojadinović, D. Stanković, B. Šljukić, FeM/rGO (M = Ni and Cu) as bifunctional oxygen electrode, Fuel 368 (2024) 131654, https://doi.org/10.1016/j.fuel.2024.131654.

[55] J. Milikić, A. Nastasić, S. Knežević, L. Rakočević, S. Stojadinović, D. Stanković, B. Šljukić, Efficient nano-size ZnM/rGO (M = Ni, Cu, and Fe) electrocatalysts for oxygen electrode reactions in alkaline media, Int. J. Hydrogen Energy 97 (2025) 247–258, https://doi.org/10.1016/j.ijhydene.2024.11.406.

[56] J. Milikić, S. Stojanović, L. Damjanović-Vasilić, R. Vasilić, L. Rakočević, S. Lazarević, B. Šljukić, Porous cerium-zeolite bifunctional ORR/OER electrocatalysts in alkaline media, J. Electroanal. Chem. 944 (2023) 117668, https://doi.org/10.1016/j.jelechem.2023.117668.

[57] J. Milikić, S. Knežević, M. Ognjanović, D. Stanković, L. Rakočević, B. Šljukić, Template-based synthesis of Co_3O_4 and Co_3O_4/SnO_2 bifunctional catalysts with enhanced electrocatalytic properties for reversible oxygen evolution and reduction reaction, Int. J. Hydrogen Energy 48 (2023) 27568–27581, https://doi.org/10.1016/j.ijhydene.2023.03.433.

[58] A.K. Shringi, R. Kumar, N.F. Dennis, F. Yan, Two-Dimensional Tellurium Nanosheets for the Efficient Nonenzymatic Electrochemical Detection of H_2O_2, Chemosensors 12 (2024) 17, https://doi.org/10.3390/chemosensors12020017.

[59] S. Baluta, F. Meloni, K. Halicka, A. Szyszka, A. Zucca, M.I. Pilo, J. Cabaj, Differential pulse voltammetry and chronoamperometry as analytical tools for epinephrine detection using a tyrosinase-based electrochemical biosensor, RSC Adv. 12 (2022) 25342–25353, https://doi.org/10.1039/d2ra04045j.

[60] S. Zhuo, M. Shao, Q. Zhou, F. Liao, Preparation, characterization, and electrochemical properties of lithium vanadium oxide nanoribbons, Electrochim. Acta 56 (2011) 6453–6458, https://doi.org/10.1016/j.electacta.2011.04.132.

[61] M. Sreejesh, S. Shenoy, K. Sridharan, D. Kufian, A.K. Arof, H.S. Nagaraja, Melt quenched vanadium oxide embedded in graphene oxide sheets as composite electrodes for amperometric dopamine sensing and lithium ion battery applications, Appl. Surf. Sci. 410 (2017) 336–343, https://doi.org/10.1016/j.apsusc.2017.02.246.